Supporting Information

Araya et al. 10.1073/pnas.1209751109

SI Text

WW Domain Phage Display, Selection, and Sequencing Library Construction. We performed the phage display and selection as described previously (1). Briefly, we displayed a 56-residue fragment of the hYAP65 protein as a C-terminal fusion to the coat protein of T7 bacteriophage (2). The WW domain fragment was generated by PCR from oligonucleotides doped with 2.1% (molar) non-WT nucleotide at each position within the 34-residue variable region (Trilink). This diversity library was cloned into the T7Select 10–3b phage display vector and used to construct a phage library using the manufacturer's instructions (Novagen/EMD Chemicals). Three rounds of selection of the WW domain library against the GTPPPPYTVG peptide bound to magnetic beads were carried out as described. High-throughput sequencing libraries were prepared using PCR and then sequenced on an Illumina GAIIx instrument. The forward primer sequence was *gctcggggatccgaattctgagatcccagac*, and the reverse primer sequence was *cggagcggtaacgttcatctgagacagcatagcttt*.

High-Throughput Sequencing and Quality Filtration. The 102-base variable region was sequenced using partially overlapping reads to increase quality (1). The data were analyzed using the Enrich software package (3). Forward and reverse read pairs were fused together. In the overlapping region, the two reads were compared. Where there was disagreement between the two reads, the base with the higher quality score was used. If the quality scores were equal, preventing identification of the correct base, the read pairs were removed from the dataset. The sequences outside the overlap region were appended to create a fused 102-base sequence. Quality scores for overlap positions where the two reads agreed were multiplied. The fused sequences were filtered for a mean Phred quality score of at least 20. To generate the final quality-filtered set, the fused sequences were compared with the WT DNA sequence, and those fused sequences with more than three consecutive mutations or more than seven total mutations were removed. The multiple sequencing replicates were found to be highly reproducible ($R^2 > 0.98$). Therefore, these multiple sets were combined into a single dataset (Table S1). Variants (unique protein sequences) within each of the combined datasets were identified and enumerated. Variants that disappeared from the input library after selection were not included. The frequency, ${}_V F_k^{unc}$, of each variant, V, at each kth round of selection was calculated as indicated in Fig. S2*A*.

Calculation of Variant Functional Scores. We took advantage of consecutive rounds of selection when calculating functional scores from variant frequencies by using a linear model-based approach. First, frequencies for each variant, V, were adjusted for nonspecific carryover. The nonspecific carryover rate was estimated using the performance of variants containing stop codons. Stop codon-containing variants should be nonfunctional, and therefore, their persistence through selection is a good estimate of nonspecific carryover (4, 5). The nonspecific carryover rate from the $k-1$th to the kth round (λ_κ) is the ratio of the frequencies of stop codon-containing sequences between the input ($\Psi_{\kappa-1}$) and output (Ψ_κ) populations (Fig. S2*A*). We used λ_κ to produce corrected input (${}_V F_k^{inp}$) and output (${}_V F_k^{out}$) frequencies for each variant that represent the abundance of variants participating specifically in the selection at each round. Using these corrected frequencies, we calculated the specific enrichment ratio for each variant at each round (${}_V F_k^{out} / {}_V F_k^{inp}$). Next, we projected the cumulative enrichment of each variant (${}_V M_k^{prj}$) through the multiple rounds of selection by constructing a linear model with the corrected enrichment ratios for all three rounds of selection. The slope of the line (S_V) is proportional to variant function; variants that enrich throughout the selection have positive slopes, whereas variants that deplete have negative slopes. We scaled the slope of each variant, S_V, by the wild type (WT) slope, S_{wt}, to calculate the variant functional score, W_V, and therefore (Eq. **S1**),

$$W_V = 2^{S_V - S_{wt}}. \quad \textbf{[S1]}$$

To remove variants that behaved erratically from our analysis, we imposed a minimum R^2 value of 0.75 for the linear model. This cutoff was applied to doubly mutated variants in all epistasis analysis and singly mutated variants in the analysis of single-mutation effects (partner potentiation is discussed below). Applying this cutoff to all variants tracked in our assay only marginally improved the predictions of the product epistasis model ($R^2 = 0.72$) (Fig. S6*B*) and yields an 80% concordant list of candidate-stabilizing mutations (Fig. S6*F*). Because such treatment reduces the number of epistasis scores to 3,548 (from 5,010) and concomitantly reduces the number of individual mutations analyzed to 159 (from 192), we refrained from enforcing this cutoff on component singly mutated variants in the calculation of epistasis scores.

Calculation of Epistasis Scores. To measure epistatic interactions between pairs of mutations (a, b), we used the functional score for the double mutant, W_{ab}, and the functional scores of variants containing only the individual mutations, W_a and W_b. Epistasis scores were calculated as the deviation observed in the double-mutant functional score, W_{ab}, from the predicted functional score arising between noninteracting mutations as specified by a neutrality model. We calculated epistasis scores between pairs of mutations (a, b) under four common neutrality models [reviewed in the work by Mani et al. (6)] of product (ε_{ab}^{pro}) (Eq. **S2**), logarithmic (ε_{ab}^{log}) (Eq. **S3**), minimal (ε_{ab}^{min}) (Eq. **S4**), and additive (ε_{ab}^{add}) (Eq. **S5**):

$$\varepsilon_{ab}^{pro} = W_{ab} - W_a \bullet W_b, \quad \textbf{[S2]}$$

$$\varepsilon_{ab}^{log} = W_{ab} - \log_2\left(\left(2^{W_a} - 1\right) \bullet \left(2^{W_b} - 1\right) + 1\right), \quad \textbf{[S3]}$$

$$\varepsilon_{ab}^{min} = W_{ab} - \min(W_a, W_b), \text{ and} \quad \textbf{[S4]}$$

$$\varepsilon_{ab}^{add} = W_{ab} - (W_a + W_b - 1). \quad \textbf{[S5]}$$

We found that the product and logarithmic neutrality models produced nearly equivalent results and best explained the combined effects of mutations in double-mutant functional scores (Fig. S3). Thus, they provided the most conservative estimates of epistasis. For all subsequent analysis of epistasis, we chose to use the product model-derived epistasis scores (ε_{ab}^{pro}) as our measure of epistasis (ε_{ab}) for its simplicity and power to explain the combined effects of mutations. Finally, we determined the mean epistasis score for each individual mutation (a) as the mean of the epistasis scores for all double mutants harboring the mutation ($\varepsilon_{ab_1}, \varepsilon_{ab_2}, \ldots \varepsilon_{ab_x}$).

Calculation of Partner Potentiation. A number of studies have shown that epistasis is linked to protein stability (7–10). To infer stabilizing mutations from epistasis scores, we developed a metric,

partner potentiation, that quantifies the degree to which an individual mutation (a) improves or potentiates the function imparted by its partner mutations (b_1, b_2, … b_x) in the collection (AB) of double mutants in which it participates (ab_1, ab_2, … ab_x). In a given double mutant (ab), the individual mutation a has a partner-normalized epistasis score with another mutation b ($P_{a\to b}$) calculated as (Eq. **S6**)

$$P_{a\to b} = \frac{W_{ab} - W_a \bullet W_b}{W_b}. \qquad \textbf{[S6]}$$

The partner potentiation score of an individual mutation (PP_a) is calculated as the mean of the partner-normalized epistasis scores for each mutation (b) in the collection (B) of partner mutations (Eq. **S7**),

$$PP_a = \frac{\sum P_{a\to b}}{N_B}, \qquad \textbf{[S7]}$$

where N_B is the number of partner mutations. We calculated partner potentiation scores for mutations that occurred in at least 10 double mutants.

Network Construction and Representation. To project epistatic interactions as a graph, we used Cytoscape (http://cytoscape.org) to diagram individual mutations as nodes in an epistasis network, where edges represent epistatic interactions (11). The graph was constructed with epistasis data from 5,010 epistasis measurements involving 314 mutations. Mutations were ordered clockwise by position. For visual clarity, only 699 epistatic interactions with values 1 SD (SD = 0.65) from the mean epistasis score ($\bar{\varepsilon} = 0.07$) are shown. Edge color intensity (value) scales with distance from the mean in the positive (red hues) and negative (blue hues) directions, with intensity cutoffs applied for epistasis scores (ε_{ab}) greater than 5.00 or below −2.50, respectively. Node color reflects the functional impact of a mutation, with blue and red representing deleterious and beneficial mutations, respectively. A blue intensity cutoff was applied for mutations (a) with functional score (W_a) below 0.5.

FoldX Analysis. We used the FoldX software suite to predict the thermodynamic impact of mutations within the hYAP65 WW domain (3). To carry out FoldX predictions, the < BuildModel > command was executed on the 1K9Q Protein Data Bank structure. The FoldX Dif_BuildModel output was parsed to recover the total_energy values for each mutation, representing the difference in folding energy between the mutation and the corresponding WT/reference (with positive numbers indicating lower stability). The output for an all-residue scan of the WW domain is available in Dataset S1. The predicted total_energy changes for the A20R, L30K, and D34T known stabilizing mutations are 0.84, 0.82, and 0.83, respectively.

Chemical Synthesis of hYAP65 WW Domain Variants. hYAP65 WW domain variants were manually chemically synthesized on a solid phase support using a fluorenylmethyloxycarbonyl (FMOC) amino terminal and tertiary-butyl side chain protecting group strategy previously reported (12). Novasyn TGT resin preloaded with Fmoc-Lys(Boc) attached by way of an acid-sensitive 4-carboxytrityl linker was used for chain elongation using Fmoc-protected α-amino acids from EMD Biosciences. Amino- and side chain-protected (where appropriate) amino acids were activated by 2-(1H-benzotriazole-1-yl)-1,1,3,3-tetramethyluronium hexafluorophosphate and *N*-hydroxybenzotriazole hydrate purchased from Advanced ChemTech. Piperidine and *N*,*N*-diisopropylethylamine were purchased from Aldrich.

WW domains prepared on a 25-μmol scale were cleaved from the resin by stirring the resin-tethered protein for ~4 h in a solution of phenol (0.5 g), water (500 μL), thioanisole (500 μL), ethanedithiol (250 μL), and triisopropylsilane (100 μL) in TFA (8 mL). Under these conditions, the acid-labile side chain-protecting groups were also globally removed. Peptides were precipitated from the TFA solution by the addition of diethyl ether (~45 mL). Peptides were purified by preparative reverse-phase HPLC using a C18 column and a linear gradient of increasing acetonitrile relative to water, with both solvents containing 0.2% vol/vol TFA. The chemical structure of the WW domain variants was confirmed by MALDI-TOF, and their purity was ascertained by C18 analytical HPLC using the buffer system used for preparative purification (Table S2).

Far UV Circular Dichroism Spectroscopy Studies. Both circular dichroism (CD) spectra and thermal denaturation curves were recorded on an Aviv 202SF CD spectrometer using quartz cuvettetes with a 1.0 cm path length. Solutions of WW domains were prepared in 20 mM sodium phosphate buffer (pH 7). WW domain concentrations were determined by UV spectroscopy on the basis of tyrosine and tryptophan absorbance at 280 nm in 6 M guanidine hydrochloride in the specified phosphate buffer (ε_{Trp} = 5,690 $M^{-1}cm^{-1}$, ε_{Tyr} = 1,280 $M^{-1}cm^{-1}$) (13). Far UV CD spectra were obtained by monitoring molar ellipticity from 260 to 200 nm at both 2 °C and 25 °C with 5 s averaging times. Variable temperature CD data were obtained by monitoring molar ellipticity at 230 nm from 0.2 °C to 88.2 °C at 2 °C intervals, with 90 s equilibration time between data points using 30 s averaging times. After the highest temperature was reached, the sample was cooled to 2 °C in 10 min, and another full CD spectrum was measured to ensure that folding was reversible. In cases where clear pre- and posttransition baselines were visible, the variable temperature CD data were fit to the following equations for two-state thermally induced unfolding transitions (in cases where pretransition baselines were not available, the melting temperatures are estimated as the middle point of the transition):

$$\Theta(T) = \Theta_F(T) + K_u \times \Theta_U(T) \Big/ 1 + K_u, \qquad \textbf{[S8]}$$

$$\Theta_F(T) = m + n \times T, \text{ and} \qquad \textbf{[S9]}$$

$$\Theta_U(T) = p + q \times T, \qquad \textbf{[S10]}$$

where T is temperature in Kelvin, the folded and unfolded CD baselines $\Theta_F(T)$ and $\Theta_U(T)$ are assumed to be linear functions of T, and K_u is the equilibrium constant for unfolding. K_u is related to the temperature-dependent free energy of folding $\Delta G_f(T)$ according to the following equation (Eq. **S11**):

$$K_u = exp\left[\Delta G_f(T) \Big/ RT\right]. \qquad \textbf{[S11]}$$

The midpoint of the thermal unfolding transition T_m (melting temperature) was calculated by fitting $\Delta G_f(T)$ to the following equation derived from the van't Hoff relationship (Eq. **S12**),

$$\Delta G_f(T) = \left[\Delta H_f(T_m) \Big/ T_m\right] \bullet (T_m - T) + \Delta C_p \left[T - T_m - T \bullet ln\left(T \Big/ T_m\right)\right], \qquad \textbf{[S12]}$$

where $\Delta H_f(T_m)$ is the enthalpy changes at T_m and ΔC_p is the heat capacity change associated with folding. ΔC_p is assumed to be temperature-independent and treated as a global fitting parameter, because the side chain mutations studied here are not expected to change the hydrophobicity of the protein. T_m and other

relevant thermodynamic parameters were obtained for each peptide as parameters of the fit. T_m and ΔG_f values listed for each peptide were obtained by averaging the T_m and ΔG_f (calculated at 323.15 K using Eq. **S12**) values from each of the three or more replicate CD melting experiments for a specific variant (Table S2). The SE for T_m and ΔG_f were calculated to estimate uncertainty in the T_m and ΔG_f values by propagation of error.

The fraction folded (F_f) at each temperature was calculated using Eq. **S13**,

$$F_f = (\sigma_{obs} - \sigma_U) \Big/ (\sigma_F - \sigma_U), \qquad \textbf{[S13]}$$

where σ_{obs} is the observed ellipticity at 230 nm and σ_F and σ_U are the ellipticities of the folded and unfolded states derived from the baselines.

1. Fowler DM, et al. (2010) High-resolution mapping of protein sequence-function relationships. *Nat Methods* 7:741–746.
2. Dai M, et al. (2008) Using T7 phage display to select GFP-based binders. *Protein Eng Des Sel* 21:413–424.
3. Fowler DM, Araya CL, Gerard W, Fields S (2011) Enrich: Software for analysis of protein function by enrichment and depletion of variants. *Bioinformatics* 27:3430–3431.
4. Jolma A, et al. (2010) Multiplexed massively parallel SELEX for characterization of human transcription factor binding specificities. *Genome Res* 20:861–873.
5. Zhao Y, Granas D, Stormo GD (2009) Inferring binding energies from selected binding sites. *PLoS Comput Biol* 5:e1000590.
6. Mani R, St Onge RP, Hartman, JL, 4th, Giaever G, Roth FP (2008) Defining genetic interaction. *Proc Natl Acad Sci USA* 105:3461–3466.
7. Bloom JD, Arnold FH (2009) In the light of directed evolution: Pathways of adaptive protein evolution. *Proc Natl Acad Sci USA* 106(Suppl 1):9995–10000.
8. Bershtein S, Segal M, Bekerman R, Tokuriki N, Tawfik DS (2006) Robustness-epistasis link shapes the fitness landscape of a randomly drifting protein. *Nature* 444:929–932.
9. Wang X, Minasov G, Shoichet BK (2002) Evolution of an antibiotic resistance enzyme constrained by stability and activity trade-offs. *J Mol Biol* 320:85–95.
10. Weinreich DM, Delaney NF, Depristo MA, Hartl DL (2006) Darwinian evolution can follow only very few mutational paths to fitter proteins. *Science* 312:111–114.
11. Shannon P, et al. (2003) Cytoscape: A software environment for integrated models of biomolecular interaction networks. *Genome Res* 13:2498–2504.
12. Ferguson N, Johnson CM, Macias M, Oschkinat H, Fersht A (2001) Ultrafast folding of WW domains without structured aromatic clusters in the denatured state. *Proc Natl Acad Sci USA* 98:13002–13007.
13. Edelhoch H (1967) Spectroscopic determination of tryptophan and tyrosine in proteins. *Biochemistry* 6:1948–1954.

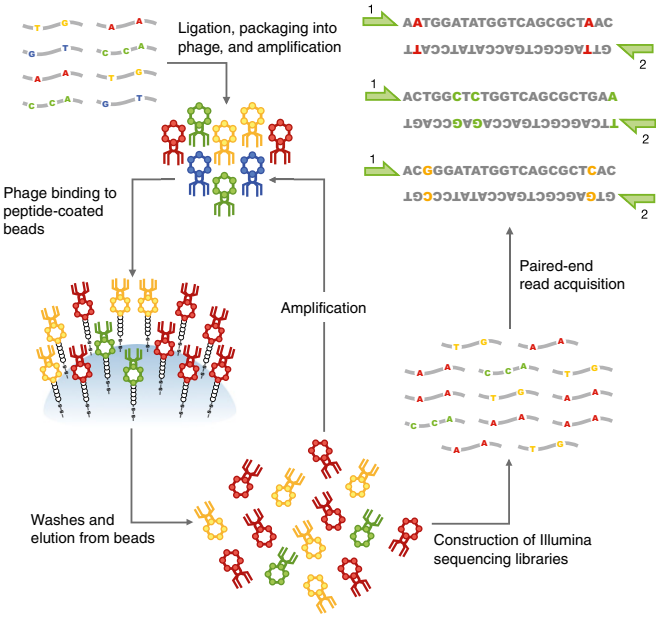

Fig. S1. Deep mutational scanning of a WW domain. A library of sequences encoding variant WW domains was generated using chemical DNA synthesis with doped nucleotide pools, PCR-amplified, and displayed as a fusion to T7 capsid protein. The input phage library was subjected to successive rounds of selection. Each round consisted of phage binding to peptide ligand immobilized on beads, washing to remove unbound phage, and elution and amplification of bound phage. Sequencing libraries were created using PCR from input phage and phage after each round of selection, and they were sequenced using partially overlapping paired-end reads on the Illumina platform. An example of four unique variants of differing affinity, each a different color, is shown. Green arrows indicate locations of sequencing primers.

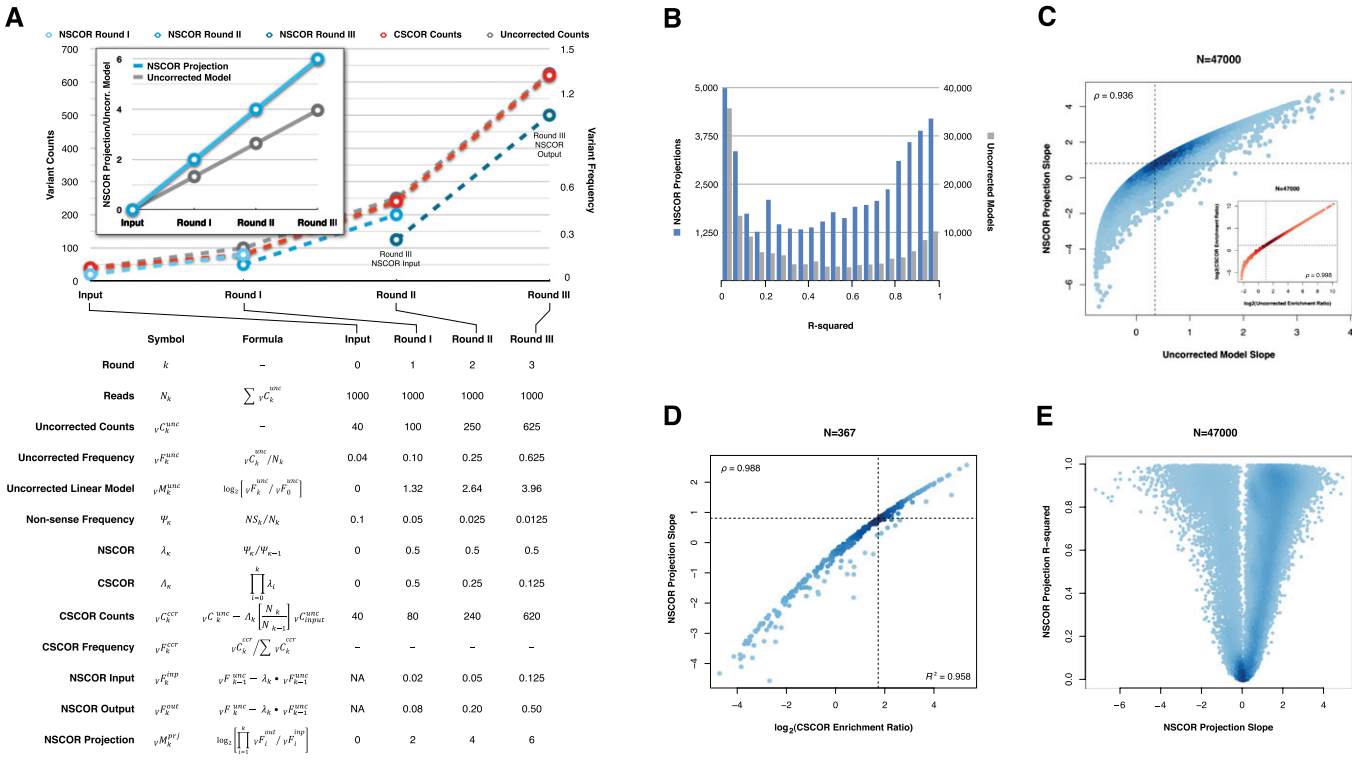

	Symbol	Formula	Input	Round I	Round II	Round III
Round	k	–	0	1	2	3
Reads	N_k	$\sum {}_V C_k^{unc}$	1000	1000	1000	1000
Uncorrected Counts	${}_V C_k^{unc}$	–	40	100	250	625
Uncorrected Frequency	${}_V F_k^{unc}$	${}_V C_k^{unc} / N_k$	0.04	0.10	0.25	0.625
Uncorrected Linear Model	${}_V M_k^{unc}$	$\log_2\left[{}_V F_k^{unc} / {}_V F_0^{unc}\right]$	0	1.32	2.64	3.96
Non-sense Frequency	Ψ_κ	NS_k / N_k	0.1	0.05	0.025	0.0125
NSCOR	λ_κ	$\Psi_\kappa / \Psi_{\kappa-1}$	0	0.5	0.5	0.5
CSCOR	Λ_κ	$\prod_{i=0}^{k} \lambda_i$	0	0.5	0.25	0.125
CSCOR Counts	${}_V C_k^{ccr}$	${}_V C_k^{unc} - \Lambda_k \left[\frac{N_k}{N_{k-1}}\right] {}_V C_{input}^{unc}$	40	80	240	620
CSCOR Frequency	${}_V F_k^{ccr}$	${}_V C_k^{ccr} / \sum {}_V C_k^{ccr}$	–	–	–	–
NSCOR Input	${}_V F_k^{inp}$	${}_V F_{k-1}^{unc} - \lambda_k \bullet {}_V F_{k-1}^{unc}$	NA	0.02	0.05	0.125
NSCOR Output	${}_V F_k^{out}$	${}_V F_k^{unc} - \lambda_k \bullet {}_V F_{k-1}^{unc}$	NA	0.08	0.20	0.50
NSCOR Projection	${}_V M_k^{prj}$	$\log_2\left[\prod_{i=1}^{k} {}_V F_i^{out} / {}_V F_i^{inp}\right]$	0	2	4	6

Fig. S2. Correction of enrichment ratios for nonspecific carryover. Deep mutational scanning relies on selection followed by sequencing to determine variant abundance. Selections for protein function have nonspecific carryover that, in the case of the assay presented here, arises primarily from incomplete washing and nonspecific phage affinity for beads. We compared two approaches to correct for nonspecific carryover using a cumulative non-specific carry-over rate (CSCOR) and a round-by-round normalized non-specific carry-over rate (NSCOR). (*A*) Correction for nonspecific carryover is shown for a variant in a hypothetical selection. *Upper* shows the raw variant abundance (gray) as well as the abundance after correction by CSCOR (red) and NSCOR (blue) methods. *Lower* shows sample calculations for the hypothetical variant (*V*) as well as the accompanying equations for corrections. Briefly, uncorrected (*Upper*, gray dashed line) and CSCOR-corrected (*Upper*, red dashed line) variant abundances are plotted from ${}_V C_k^{unc}$ and ${}_V C_k^{ccr}$ counts, respectively. CSCOR-corrected frequencies are not listed, because these values depend on the number of variants removed by the correction. In *Upper*, the dashed blue lines indicate the round-specific NSCOR-corrected input $({}_V F_k^{inp})$ and output $({}_V F_k^{out})$ frequencies. For each round, a corrected enrichment term $({}_V F_k^{out} / {}_V F_k^{inp})$ is calculated from the NSCOR-adjusted frequencies, and the product of these terms is used to project the NSCOR-adjusted enrichment of the variant through selection, hereafter referred to as the NSCOR projection model (*Upper Inset*, solid blue line, ${}_V M_k^{prj}$). For comparison, the sequential uncorrected linear model is shown as well (*Upper Inset*, solid gray line, ${}_V M_k^{unc}$). (*B*) A histogram of the R^2 values for the NSCOR-corrected projections and uncorrected linear models are shown. NSCOR correction significantly improves the fit. (*C*) A plot of the NSCOR-corrected projection vs. the uncorrected linear model slope is shown for each variant. *Inset* shows a plot of the CSCOR-corrected round 3 enrichment ratio $(\log_2[{}_V F_3^{ccr} / {}_V F_0^{ccr}])$ vs. the uncorrected round 3 enrichment ratio $(\log_2[{}_V F_3^{unc} / {}_V F_0^{unc}])$ for each variant present in both the NSCOR- and CSCOR-corrected datasets. Spearman's ρ is shown for both *C* and *C Inset*. Dashed lines indicate the respective scores for the WT sequence. (*D*) A plot of the NSCOR projection slope vs. the CSCOR-corrected enrichment ratio for singly mutated variants present in both datasets is shown. The Spearman's ρ (upper left corner) and Pearson's R^2 (lower right corner) show a very strong correlation between the two metrics of function. Dashed lines indicate the respective scores for the WT sequence. (*E*) For each variant, the NSCOR projection slope is plotted vs. the R^2 value of the linear model. As expected, models with small R^2 values have slopes near zero.

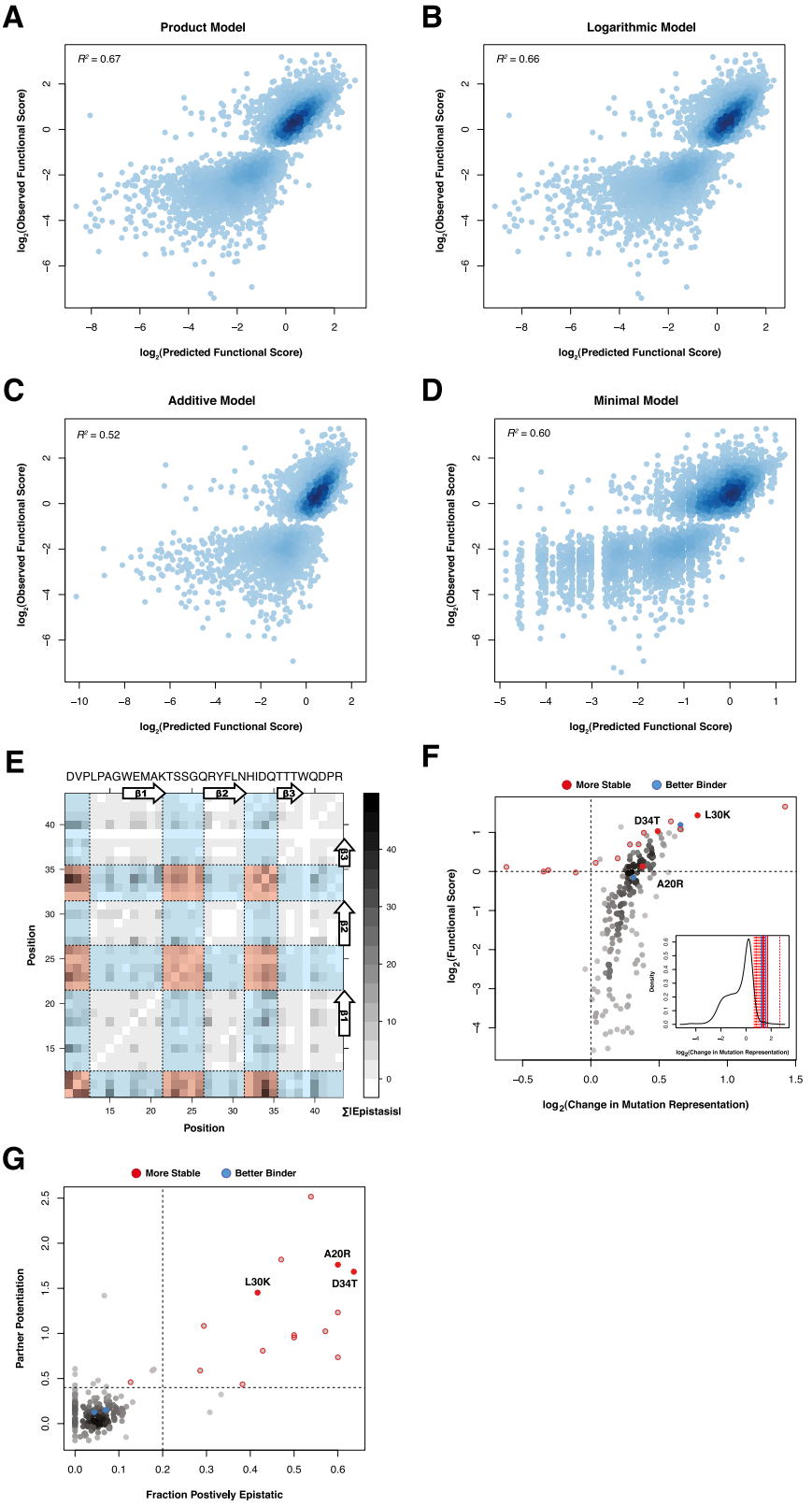

Fig. S3. Modeling neutrality, population-level epistasis, and signatures of stabilizing mutations from large-scale functional data. (*A–D*) Each of the four major neutrality models for calculating epistasis was used to predict doubly mutated variant functional scores from the component singly mutated variant functional scores. The product (*A*), logarithmic (*B*), additive (*C*), and minimal (*D*) models are shown. In each case, the Pearson's R^2 is calculated. The additive model produced epistasis scores < 0 in some cases. These points are omitted from the plot, because they cannot be displayed on a logarithmic scale. (*E*) Spatial analysis of epistasis in the WW domain. For each pair of positions (*i*, *j*) in the WW domain, we graphed the sum of the absolute epistasis scores of double mutants with mutations in *i* and *j*. To examine spatial enrichment of epistasis, we calculated the intensity of epistasis between pairs of positions (*i*, *j*) by normalizing the sum of the absolute epistasis scores of double mutants with mutations in *i* and *j* by the number of double mutants with mutations in *i* and *j*. We found three regions

Legend continued on following page

(collectively spanning positions 10–12, 22–26, and 32–35) where epistasis is significantly higher than in the rest of the protein (colored vs. gray regions; Wilcoxon rank sum test $P = 7.85 \times 10^{-22}$). Similarly, epistasis is significantly enriched within these regions (red vs. blue regions; Wilcoxon rank sum test $P = 1.78 \times 10^{-14}$). (*F*) Enrichment of mutations within the double-mutant population after selection is not a good predictor of stability. For each mutation (m_x) in the unselected and round three libraries, we tabulated the fraction (f) of doubly mutated variants that harbored m_x. Thus, *f(round 3, m_x)* represents the fraction of the doubly mutated variants at round three that have the m_x mutation. Next, we calculated the fold change in representation for each m_x mutation as *f(round 3, m_x)/f(unselected, m_x)* and plotted the density of these log-transformed ratios for all individual mutations (*Inset*). This process overcomes the biases in sequence frequency for each amino acid substitution that are caused by the genetic code. Red and blue solid lines denote known stabilizing and activating mutations, respectively. Additional candidate stabilizing mutations determined by partner potentiation are shown in dashed red lines. The fold change in representation (log-transformed) is plotted against functional score for each of the 192 mutations found in 10 or more double mutants in *F*. The known stabilizing mutations (A20R, L30K, and D34T) and affinity-enhancing mutations (K21R and Q35R) are represented as red and blue points, respectively. The candidate stabilizing mutations selected on the basis of partner potentiation and functional scores are circled in red. (*G*) Doubly mutated variants harboring high partner potentiation single mutations frequently have positive epistasis scores. Partner potentiation for each of the 192 mutations found in 10 or more double mutants is plotted against the fraction of double mutants containing the mutation that has positive epistasis scores (≥1 SD from the mean). The known stabilizing mutations (A20R, L30K, and D34T), and affinity-enhancing mutations (K21R and Q35R) are represented as red and blue points, respectively. The candidate stabilizing mutations selected on the basis of partner potentiation and functional scores are circled in red.

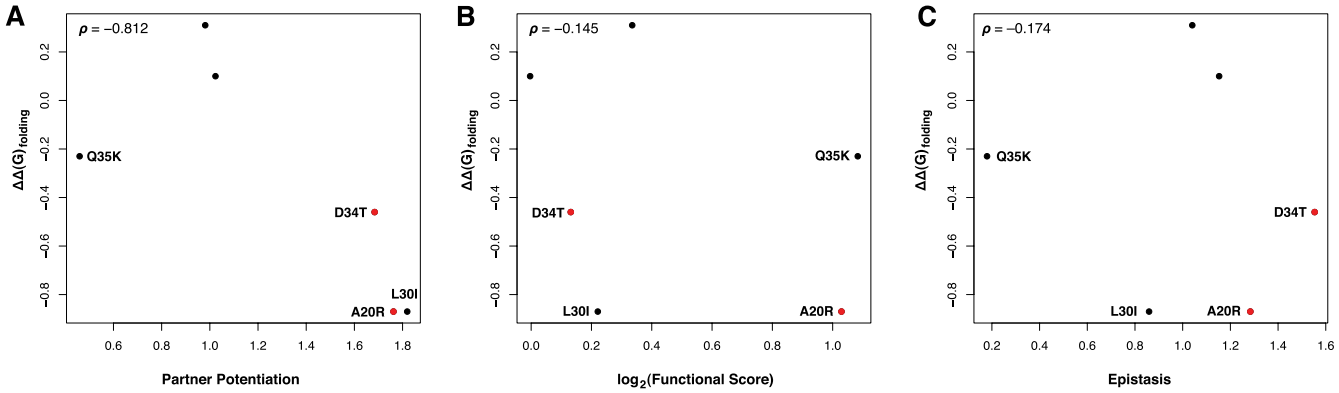

Fig. S4. Partner potentiation and $\Delta\Delta G_{folding}$ are inversely correlated. Partner potentiation (*A*), single-mutant functional score (*B*), and epistasis (*C*) are plotted vs. $\Delta\Delta G_{folding}$ as measured by thermal denaturation for chemically synthesized WW domains bearing candidate stabilizing mutations in either this work (L30I, D34T, Q35K, I33R, T36R) or the work by Jiang et al. (1) (A20R). Thermostability is highly correlated with partner potentiation score (Spearman's $\rho = -0.81$) but not single-mutant functional score or epistasis.

1. Jiang X, Kowalski J, Kelly JW (2001) Increasing protein stability using a rational approach combining sequence homology and structural alignment: Stabilizing the WW domain. *Protein Sci* 10:1454–1465.

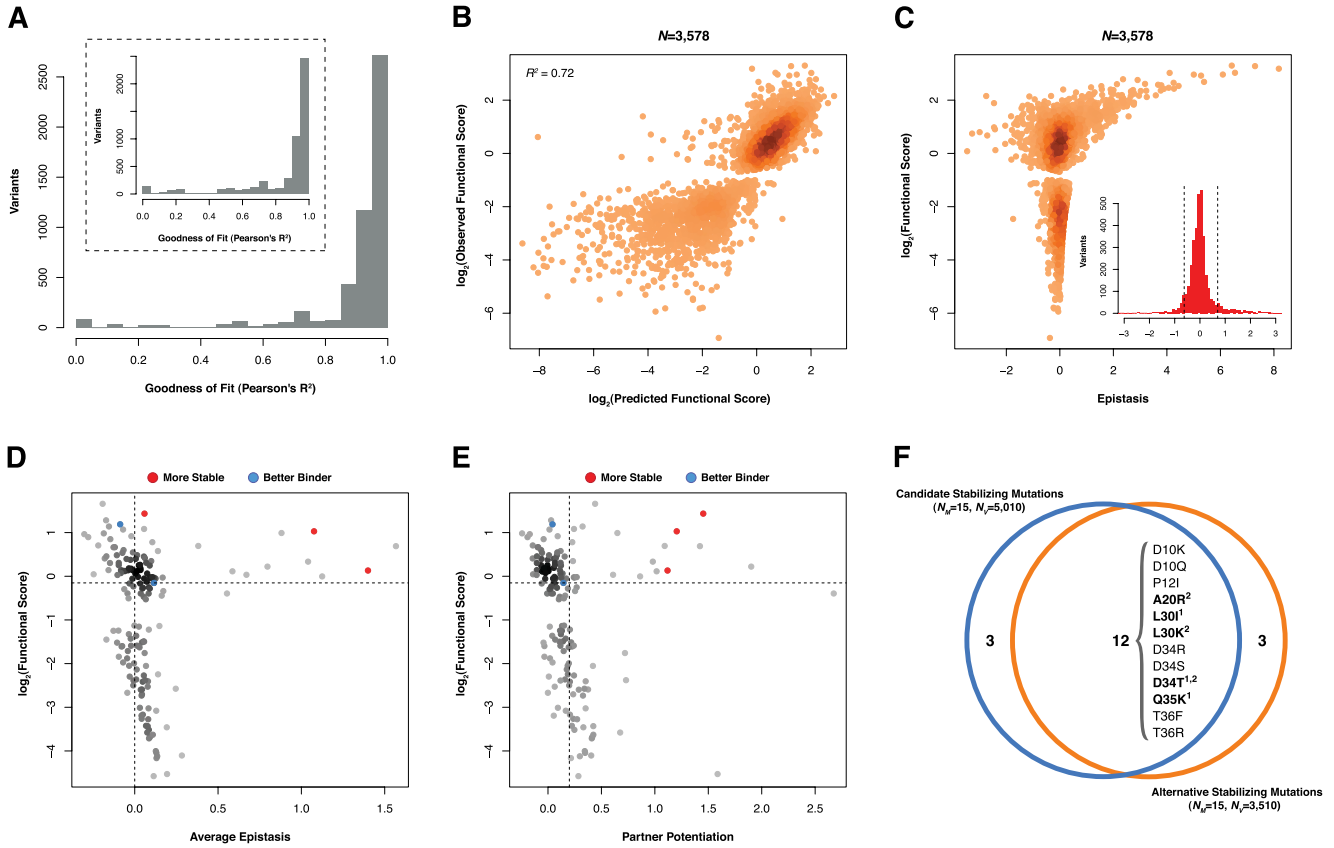

Fig. S5. Stability analysis is robust to increased stringency in variant selection. To address the robustness of our measurements, we repeated our epistasis and stability analysis using a more stringently filtered set of trios, where double- and single-mutant variants comply with a goodness-of-fit cutoff of $R^2 \geq 0.75$. Using this more stringently filtered set of variants, we calculate 3,548 epistasis scores and analyze the effects of 159 individual mutations. (*A*) Histograms of *a* and *b* mutation R^2 values in trios containing 5,010 *ab* double mutants with an $R^2 \geq 0.75$ as analyzed in the text. (*B*) The functional score of 3,548 doubly mutated variants was predicted from the functional score of the component singly mutated variants using the product model. The predicted functional score is plotted against observed functional score and similarly correlated (Pearson's $R^2 = 0.72$). (*C*) Epistasis scores calculated using the product model for the 3,548 variants are plotted against the functional score of the doubly mutated variant. The distribution of epistasis scores is shown in *Inset*. Dashed lines are placed at ±1 SD from the mean. (*D*) The average epistasis score of each of the 159 single mutants found in 10 or more double mutants is plotted against the single-mutant functional score of each mutation. The known stabilizing (A20R, L30K, and D34T) and activity-enhancing (K21R and Q35R) mutations are highlighted in red and blue, respectively. (*E*) Partner potentiation is plotted for each single mutation against its functional score. The known stabilizing (A20R, L30K, and D34T) and activity-enhancing (K21R and Q35R) mutations are highlighted in red and blue, respectively. Mutations with a partner potentiation score greater than 0.4 and a functional score greater than 0.9 were considered to be candidate stabilizing mutations for the more stringently filtered trios. (*F*) The lists of candidate stabilizing mutations as selected from the 5,010 mutations (blue circle) and 3,548 trios (orange circle) are highly concordant, with 80% of candidate stabilizing mutations from either subset being represented in both lists. Mutations with experimentally validated beneficial functional effects are highlighted in bold; 1 denotes stabilizing mutations validated in this study, 2 denotes previously identified stabilizing mutations, and 3 denotes previously identified activating mutations.

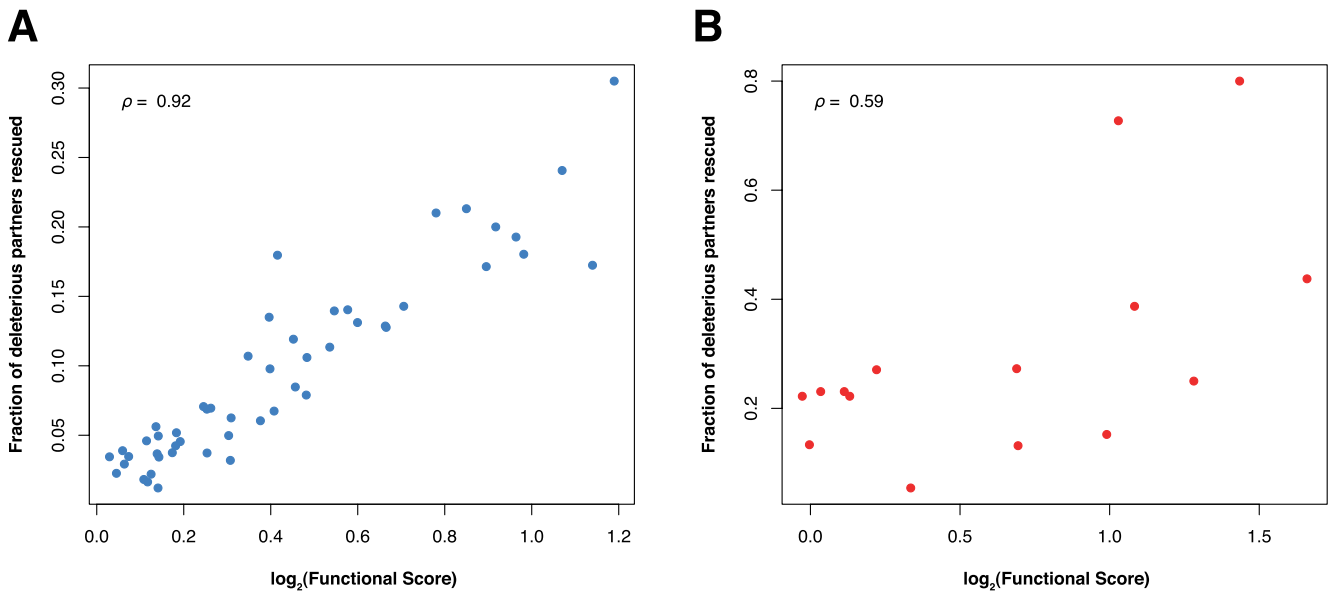

Fig. S6. Functional score is a better predictor of rescue effects among activating mutations than among stabilizing mutations. We examined the set of deleterious mutations that combined with both stabilizing and activating mutations in double mutants in the input library (n = 192). We calculated the fraction of these deleterious mutations rescued (i.e., with a double-mutant functional score that was greater than WT) by each activating and stabilizing mutation. The fraction rescued is plotted against functional score for each activating mutation (*A*) and stabilizing mutation (*B*). The difference in these correlations is significant as determined using random sampling ($P \leq 0.0001$).

Table S1. WW library sequencing and variant calling statistics

Code	Raw reads	Quality-filtered reads	Fraction passed (%)
Input	14,244,460	10,162,632	71.344
Round 1	12,592,010	8,891,303	70.611
Round 2	11,047,866	9,014,000	81.590
Round 3	15,652,575	12,772,327	81.599

Table S2. Summary statistics of candidate stabilizing mutations, physicochemical properties, and MALDI-TOF data for WW domain variants

Mutation/ sequence	Functional score	Partner potentiation	Average epistasis	Fraction positively epistatic	Fraction negatively epistatic	No. double mutants	T_m (°C)	ΔT_m (°C)	ΔG_f (kcal/mol)	$\Delta\Delta G_f$ (kcal/mol)	Expected [M+H]+ (g/mol)	Observed [M+H]+ (g/mol)
P12H	0.981	2.516	0.952	0.538	0	13	~20*	—†	—†	—†	4,718.22	4,720.39
L30I	1.166	1.819	0.859	0.471	0	17	54.8 ± 0.5	11.8 ± 0.7	−0.38 ± 0.06	−0.87 ± 0.07	4,678.19	4,679.98
A20R	2.041	1.762	1.284	0.6	0.067	15						
D34T	1.095	1.684	1.553	0.636	0	11	49.6 ± 0.4	6.6 ± 0.6	0.03 ± 0.03	−0.46 ± 0.05	4,664.21	4,664.51
L30K	2.703	1.453	0.059	0.417	0.333	12						
D10Q	1.612	1.232	1.217	0.6	0	20	~20*	—†	—†	—†	4,691.24	4,693.7
D34S	1.618	1.083	0.396	0.294	0.294	17						
I33R	0.998	1.023	1.153	0.571	0	14	41.7 ± 0.5	−1.3 ± 0.7	0.59 ± 0.04	0.10 ± 0.05	4,721.22	4,724.7
T36R	1.262	0.981	1.04	0.5	0.1	10	38.4 ± 0.6	−4.6 ± 0.8	0.80 ± 0.04	0.31 ± 0.05	4,733.28	4,735.08
P12I	1.082	0.955	0.553	0.5	0.1	10						
D10K	1.987	0.808	0.913	0.429	0.238	21						
T36F	1.024	0.736	0.728	0.6	0.1	10						
D34R	3.159	0.588	0.012	0.286	0.286	14						
Q35K	2.119	0.459	0.18	0.127	0.099	142	46.6 ± 0.6	3.6 ± 0.8	0.26 ± 0.04	−0.23 ± 0.05	4,678.24	4,683.41
D34K	2.431	0.436	0.104	0.382	0.353	34						
WT							43.0 ± 0.5	—‡	0.49 ± 0.04	—‡	4,678.19	4,679.95

Measured melting temperatures were obtained with variable temperature far-UV CD experiments on 10 μM solutions of each WW domain variant in 20 mM sodium phosphate buffer (pH 7; details in *SI Text*). Folding free energies are calculated at 323.15 K.

*For variants for which pretransition baselines could not be measured (because they were unstable), T_m values were estimated visually.

†Data were not calculable with a two-state transition model because of loss of pretransition baselines.

‡All of the ΔT_m and $\Delta\Delta G_f$ data are the difference in the T_m and ΔG_f of the variants compared with WT YAP65 WW domain.

Other Supporting Information Files

Dataset S1 (XLS)